Quantification of Boundary Layer Mixing over the Southern Ocean Using In-Situ and Remotely-Sensed Measurements

S. Hartery[1], P. Kuma[1], M. J. Harvey[2], A. J. McDonald[1]

[1]School of Physical and Chemical Sciences, University of Canterbury, Christchurch, New Zealand
[2]National Institute of Water & Atmospheric Research, Wellington, New Zealand

Key Points:

- We describe a new methodology which quantifies boundary layer mixing using measurements of suspended particle surface area
- Observations and forecasts show that the Southern Ocean boundary layer is well-mixed 92% of the time
- Optical properties of low-level Southern Ocean cloud are closely tied to the physicochemical characteristics of boundary layer particles

Corresponding author: Sean Hartery, `hartery.s.p@gmail.com`

Abstract

We demonstrate that the temporal correlation between the abundance of particulate surface area at sea–level and measurements of ceilometer backscatter can be used to quantify boundary layer mixing. Throughout an austral summer voyage to the Ross Sea, correlations between the two quantities were consistently high, identifying that the Southern Ocean boundary layer was frequently well-mixed. This provides indirect evidence that the optical characteristics of low-level Southern Ocean cloud are fundamentally related to the abundance and physicochemical properties of boundary layer particles. Following this analysis, we define simple criteria for which the boundary layer is likely to be well-mixed. We found that if sea-level wind speeds exceeded 8 m s^{-1} or if the near-surface air was 3 K cooler than the sea surface, a well-mixed boundary layer was always observed. Overall, these conditions are satisfied 92% of the time between 40–70°S based on forecasts from the Antarctic Mesoscale Prediction System.

Plain Language Summary

Particles suspended in the atmosphere (aerosol) act as seeds for cloud droplet formation. The abundance of such particles directly influences the opacity of clouds, while their physical and chemical characteristics govern if and when those cloud droplets freeze. As a result, both the amount of solar radiation a cloud can reflect back to space and thus, the temperature of waters below, are sensitive to the quantity and type of particles available. We present a new methodology for understanding the conditions in which low-level clouds have direct access to the large and diverse reservoir of particles in the surface layer. We find that conditions for mixing particles up from the surface and into low-level cloud are satisfied 92% of the time over the Southern Ocean based on regional weather forecasts. This suggests that the particles we observe near the surface almost always play a significant role in cloud formation.

1 Introduction

Despite the small scale of aerosol–cloud interactions, errors in how they are represented within global climate models can cause significant climatological biases in the radiative balance. In particular, uncertainties in predicting cloud phase lead to substantial biases in the cold sector of Southern Ocean cyclones (Bodas-Salcedo et al., 2014). While the abundant cyclones of the Southern Ocean (Irving et al., 2010) occur solely as a function of synoptic conditions, global climate model's predictions of cloud phase in the cold sector of Southern Ocean cyclones (Vergara-Temprado et al., 2018), and in the wider Southern Ocean (Schuddeboom et al., 2019), are extremely sensitive to the properties of particles in the underlying boundary layer. Understanding the conditions in which these particles can reach cloud base is therefore important in correctly predicting a cloud's optical properties.

As wind speeds have increased over the Southern Ocean (Young et al., 2011; Hande, Siems, & Manton, 2012), there is significant interest in how naturally-produced particles impact cloud formation and the optical properties of the resultant clouds (McCoy et al., 2015), and whether this interaction represents a substantial climate feedback (Korhonen et al., 2010). It is well–known that increasing the population of cloud condensation nuclei (CCN) directly increases the opacity of the overlying cloud (Twomey, 1977). Increases in winds over the region will enhance the flux of sea spray particles (SSPs) from breaking waves (Hartery et al., 2020). These particles are the only local source of ice-nucleating particles (INPs) in the Southern Ocean (DeMott et al., 2016), a region almost devoid of INPs (Bigg & Hopwood, 1963). Not only are ice clouds much less opaque (Hu et al., 2010), they are much more likely to precipitate (Borys et al., 2003). Thus, changes in the abundance of SSPs may have significant impacts on cloud radiative properties.

One of the challenges in unravelling aerosol–cloud interactions over the Southern Ocean is that the region is frequently covered in cloud (80% of the time; Haynes et al. (2011)), resulting in a sparsity of boundary layer observations from space. While observational records of radiosondes from Macquarie Island provide rich data on the thermodynamic structure of the Southern Ocean boundary layer (Hande, Siems, Manton, & Belusic, 2012), the lack of accompanying observations of CCN or INPs leaves a gap in our understanding of how these particles interact with cloud. Previous research, such as the dedicated ACE-1 (Russell et al., 1998), SOCEX (Boers et al., 1998), HIPPO (Wofsy, 2011) and more recently SOCRATES campaigns have used aircraft observations to bridge this knowledge gap. However, aircraft can only fly in a limited range of conditions, as the strong vertical wind shear and icing within boundary layer cloud present dangers. By contrast, ship–based measurements can be made in nearly all conditions. Here, we use measurements on the R/V *Tangaroa* during a voyage to the Ross Sea in 2018 to establish conditions in which particles near the surface are turbulently mixed to cloud base. Establishing conditions when sea-level measurements are relevant to cloud will enable future research to better exploit sea-level measurements in aerosol–cloud interaction studies, and adds value to near-surface measurements.

2 Measurements

Over the course of a voyage between New Zealand and the Ross Sea, a passive cavity aerosol spectrometer probe (PCASP-100X; Droplet Measurement Technologies) and a differential mobility particle sizer (DMPS, TSI) measured the ambient concentration of particles suspended in the atmosphere at 2 m a.s.l. The PCASP measured the number concentration size spectra of particles suspended in the boundary layer in 30 size bins (0.1–3.0 μm) every minute. The DMPS measured the number concentration size spectra in the size range 0.02–0.3 μm every 10 minutes. Following Modini et al. (2015) and Quinn et al. (2017), we fit three lognormal size distributions to estimate the average diameter and number concentration of Aitken, accumulation and sea spray particles. The PCASP was used exclusively to estimate the average size and abundance of SSPs, while the DMPS was used for the Aitken and accumulation particles. When data from the DMPS were not available, the PCASP was used to constrain the abundance and size of accumulation particles. Further details on sampling set-up and analysis, including correction factors for losses through the sampling line, are described in Hartery et al. (2020). We also measured the total number of cloud condensation nuclei (CCNC-100; Droplet Measurement Technologies) from the same sampling conduit that drew ambient air to the PCASP and DMPS. A measurement of the average number of ambient CCN was made twice an hour at intervals of 0.1% supersaturation between 0.2–1.0%.

A ceilometer (CHM-15K; Lufft) measured vertical profiles of attenuated backscattered light ($\lambda = 1064$ nm), β, over the R/V *Tangaroa* every minute at a resolution of 15 m. For each profile, the instrument also estimated the cloud base height (CBH). A raw quality control flag provided by the instrument was used to screen for field-of-view contamination from fog or residual precipitation on the outer optical window. A micro-rain radar (MRR-2; Metek) operated in close proximity was also used to detect and screen for precipitation events. Both fog and precipitation events were a common occurrence on this voyage (Kuma et al., 2019).

The NZ MetService's Automated Weather Station (AWS) was positioned above the bridge of the R/V *Tangaroa* at 22.5 m. Relevant measurements included ambient pressure, air temperature, relative humidity, wind speed, and wind direction.

AWS measurements were corrected to a height of 10 m as detailed in Hartery et al. (2020). The bulk seawater temperature was measured at a depth of 5.5 m below sea level with a thermistor (SBE38; Sea-Bird Scientific). We used the COARE 3.5 bulk-flux algorithms (Edson et al., 2013) to calculate the sea skin temperature from the bulk temperature.

Sixty meteorological balloons were launched during the voyage. The radiosondes (iMet-ABx; InterMet) recorded pressure, relative humidity, temperature and wind speed. The radiosondes were launched twice daily once the ship passed the 60^{th} parallel.

Regional meteorological forecasts were downloaded from the Antarctic Mesoscale Prediction System (AMPS). AMPS initializes a new forecast every twelve hours, with subsequent output provided every three hours. AMPS uses the Mellor-Yamada-Janjić (MYJ) scheme, a 2.5-level closure model of turbulence, to predict the behaviour of the planetary boundary layer (PBL). The height of the PBL predicted by AMPS is the height at which the turbulent kinetic energy falls below a pre-determined threshold (Janjić, 2001). The AMPS data used in this study were downloaded from: `https://www.earthsystemgrid.org/project/amps.html`. Following common practice (Jolly et al., 2016), only forecasts between 12–21 hours were used, which provides a 12 hour spin-up.

3 Methods

The suspended particle cross-sectional surface area, A, was calculated from the number concentration size spectra measured by the PCASP:

$$A = \int \frac{\mathrm{d}n}{\mathrm{d}\log D_p} \pi \left(\frac{D_p}{2}\right)^2 \mathrm{d}\log D_p \tag{1}$$

Where D_p is the particle diameter and n is the partial concentration of particles. The surface area is dominated by the sea spray and accumulation mode particles (97%, on average; Fig. 1d), which the PCASP can readily measure.

To quantify the boundary layer mixing state, we calculated the Spearman Rank correlation between the time-series of A (Eq. 1), and the attenuated backscatter measured by the ceilometer, $\beta(z)$. The attenuated backscatter was calculated from the raw, range-corrected signal using a nominal value for the lidar constant of 1×10^{-11}. However, the attenuated backscatter is a function not only of the backscatter coefficient of particles, but also the backscatter coefficient from molecules and the atmospheric transmission from the surface to the sample volume (and back). As such, the Spearman Rank correlation was used as the correlation coefficient, since non-linearities in the attenuated backscatter could potentially arise from variations in these other factors. These correlations were calculated over a moving window 12 hours wide. Shorter temporal windows risked correlating underlying instrument sampling noise from Poisson counting statistics. To avoid contamination from cloud backscatter, only measurements below the 10^{th}-percentile of CBH were studied. The observations were also screened based on the ceilometer's quality control flag discussed in Section 2. Since the thermal properties of seawater result in a very minor diurnal cycle in surface temperature (Schluessel et al., 1990), diurnal cycles in PBL depth are rarely observed over the open ocean. Hence, correlations between surface particulate and particulate aloft are determined by the presence of turbulence or convection alone, where high correlations indicate a well-mixed boundary layer.

To classify the boundary layer mixing state, we used two measures of atmospheric stability: the Brunt-Väisälä Frequency, N, and the vertical shear strength,

S. These were calculated from the AWS measurements and the radiosondes, where:

$$N^2 = \frac{g}{\theta_v}\frac{\partial \theta_v}{\partial z}$$
$$S^2 = \left(\frac{\partial u}{\partial z}\right)^2 + \left(\frac{\partial v}{\partial z}\right)^2 \tag{2}$$

where g is the gravitational acceleration, θ_v is the virtual potential temperature, u and v are the zonal and meridional components of the wind vector, and z the height above sea level. These measures were then used to calculate the Richardson number, Ri:

$$Ri = \frac{N^2}{S^2} \tag{3}$$

The Richardson number arises in the time-dependent equation for the development of turbulent kinetic energy, and generally predicts that turbulence will subside for large values, and strengthen for low, or negative values (Richardson, 1920). For radiosonde measurements, gradients were calculated using a 30 s wide linear Savitzky-Golay filter. For a typical balloon ascent rate of 5 m s^{-1}, this corresponds to an altitude resolution of 150 m. For AWS measurements, gradients were calculated between the 10 m level and sea-level according to the COARE 3.5 bulk-flux algorithms (Edson et al., 2013). To differentiate between the two, subscripts $_g$ and $_b$ are used to denote the gradient and bulk Richardson number. Finally, we calculated the lifted condensation level (LCL) from the AWS measurements as an estimate of CBH (Romps, 2017).

4 Results

4.1 Time Series Analysis

Throughout the voyage to and from the Ross Sea (voyage track shown in Fig. 1a), the number–size distribution of particulate was predominantly trimodal. This is consistent with previous observations in marine settings (Bates et al., 1998; Quinn et al., 2017). Particles in the smallest two modes, the Aitken (30 nm, σ = 1.4) and accumulation modes (100 nm, $\sigma = 1.6$), are concomitant. These particles are nucleated in–situ from the condensation of oxidized marine gasses and grow via self-coagulation and condensation. In contrast, sea spray particles (400 nm, $\sigma = 2$) are directly generated from breaking ocean waves, and tend to be much larger than particles in the Aitken and accumulation mode (Prather et al., 2013).

A representative size distribution of particles observed in the Southern Ocean marine boundary layer is shown in Fig. 1b. The bifurcation of the Aitken and accumulation modes occurs when these particles pass through non-precipitating cloud, since only the largest particles are activated (Hoppel et al., 1986). Previous research has shown that the supersaturation of water vapour within nascent marine stratus is relatively modest (<0.3%) (Hegg et al., 2009). An estimation of the activation diameter based on a supersaturation of 0.3%, and a range of particle hygroscopicity parameters is also shown in Fig. 1b. This coincides well with the local minimum between the Aitken and accumulation mode.

Fig. 1c displays the number of particles in both the accumulation and sea spray modes, as these are the only particles relevant to cloud formation. This is compared to the number concentration of CCN measured at a fixed supersaturation of 0.3%. As expected, these two measurements are highly correlated. Across the entire voyage, SSPs did not comprise a substantial fraction of CCN (14%). However, in the latter half of the voyage we encountered several low pressure systems. These cyclones were accompanied by high winds, resulting in substantial wave-breaking and subsequent SSP generation in the region. This led to an enhanced relevance of SSPs to CCN (20%).

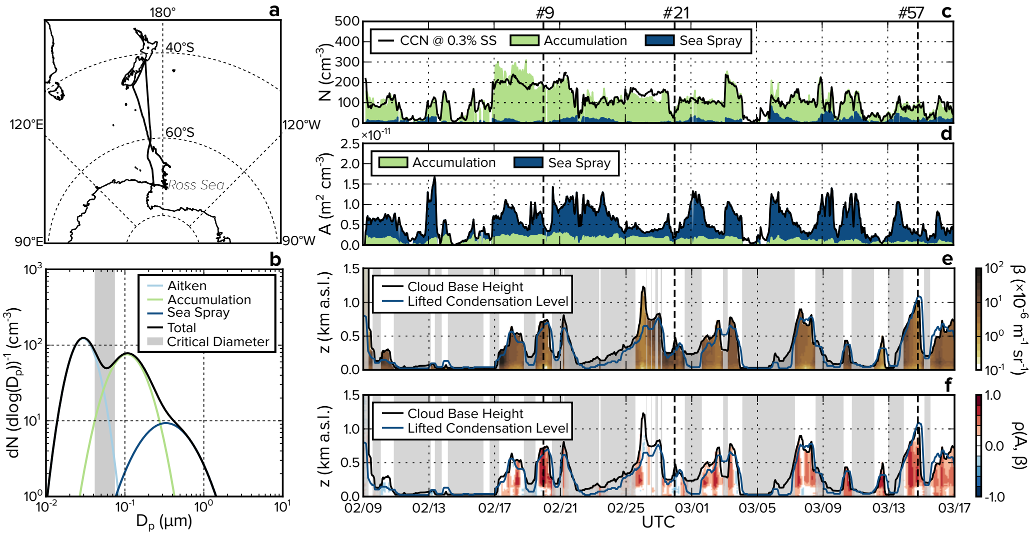

Figure 1. (a) The track of the R/V *Tangaroa* during the Marine Environment and Ecosystem Voyage. (b) A typical size distribution for particles in the Southern Ocean. The expected range of cloud activation diameters for marine stratus is shown in grey. (c) The sea-level abundance of sea spray particles (SSPs; blue filled region) and accumulation mode particles (green filled region) is compared to the abundance of cloud condensation nuclei (CCN) at a supersaturation of 0.3% (black line). (d) The abundance of suspended surface area was calculated from the measured particle size distributions (Eq. 1). (e) A contour plot of the attenuated backscatter coefficient measured by the CHM-15K ceilometer. The lifted condensation level (LCL) and cloud base height (CBH) are also shown for reference. (f) Spearman Rank correlation coefficients between the sea-level abundance of particulate surface area and ceilometer backscatter are shown. Time periods when the ceilometer optical window was obscured by precipitation or by fog are shaded.

Fig. 1d shows the abundance of suspended particle surface area. Despite the relatively low abundance of SSPs, the total amount of particulate surface area is strongly dominated by variations in their abundance. In Fig. 1e we show the time series of attenuated backscatter profiles measured by a coincident ceilometer, along with running averages of cloud base height (CBH) and the lifted condensation level (LCL). As previously discussed in (Kuma et al., 2019), the tight correspondence between CBH and the LCL over the Southern Ocean implies that CBH is primarily a function of surface temperature and relative humidity.

We used a Spearman Rank correlation analysis between suspended particle surface area at sea-level (Fig. 1d) and ceilometer backscatter from particles overhead (Fig. 1e) to assess whether our measurements at the surface were representative of the below–cloud population of CCN. Fig. 1 displays strong correlations between these two quantities throughout the voyage when fog or precipitation did not obscure the ceilometer observations. This suggests that the Southern Ocean boundary layer was consistently well-mixed throughout this measurement campaign. While correlations below 150 m seemed to be consistently weaker than aloft, this was primarily a result of the CHM-15K's sensitivity to near-field scattering. In a comparison to the NIES lidar the CHM-15K systematically under-estimated the attenuated backscatter coefficient for altitudes less than 200–300 m (Jin et al., 2018). Systematic errors in the near-range can result from a mis-calibrated lidar overlap function.

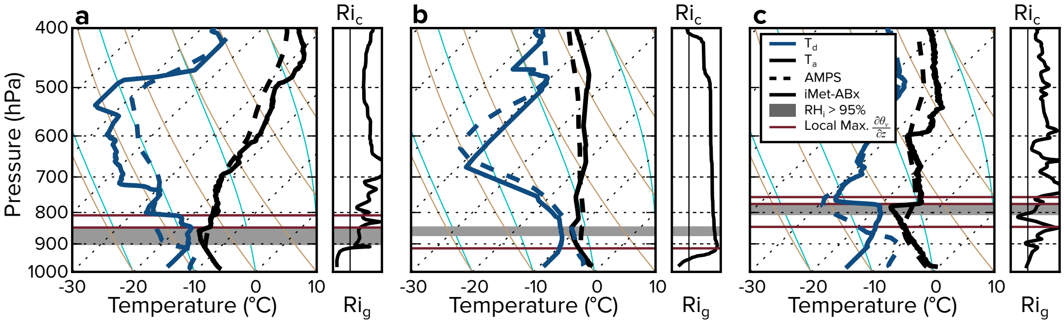

Figure 2. **a–c** The left-hand panel shows Skew Temperature – *log* Pressure plots for three different radiosondes launched from the R/V *Tangaroa* (#9, #21, and #57; see Fig. 1 for launch time). Thin cyan and gold curves represent moist and dry adiabats, respectively. Thick, solid lines represent measured values, while thick, dashed lines are forecasts from the Antarctic Mesoscale Prediction System (AMPS). Local maxima in the gradient of virtual potential temperature ($\partial\theta_v(\partial z)^{-1}$) were used to identify layer boundaries, while the relative humidity over ice (RH_i) was used to identify cloud structures. The right-hand panel of each radiosonde shows the gradient Richardson Number, Ri_g, compared to the critical Richardson number for turbulence, $\mathrm{Ri}_c = 0.25$.

4.2 Radiosonde Analysis

To validate the correlation analysis, we studied three representative radiosonde profiles from the 60 launched during the voyage. These are presented in Fig. 2a–c. The three radiosondes were selected to place our results from the correlation analysis within a more conventional analysis of boundary layer mixing. The radiosondes selected contrast conditions in which correlations between sea-level and column surface area were negative (b) and positive (a & c). To understand the state of mixing in the boundary layer, we calculated the gradient Richardson number, Ri_g, along these profiles.

Radiosonde #9 (R9), represented a classically well-mixed boundary layer (Fig. 2a). Throughout the boundary layer, values of Ri_g were low, reflecting the strong vertical wind shear present from sea-level to cloud base. This agrees with our correlation analysis, which found strong correlations that persisted up to cloud base (Fig. 1f). In contrast, the weakly negative correlations throughout the launch of R21 indicated that the boundary layer was likely decoupled from the cloud. While low near sea-level, the value of Ri_g quickly grew throughout the boundary layer due to low vertical wind shears (R21, Fig. 2b). As a result, the boundary layer decoupled from the sub-cloud layer near 925 hPa. Boundary Layer decoupling occurred in R57, too; however in this case, the decoupled boundary layer was overlaid by a strongly sheared sub-cloud layer (Fig. 2c). In contrast to R21, correlations were high throughout R57. This suggests that mixing of particulate across the below–cloud inversion during R57 was possible as a result of the weak inversion (0.6 K km^{-1}) separating the layers and large vertical shear present in both the sub-cloud layer and boundary layer ($\mathrm{Ri}_g < 0.25$). By comparison, the below-cloud inversion observed during R21 was much stronger (3 K km^{-1}); which, in addition to the lack of vertical wind shear, strongly inhibited mass transfer from the boundary layer up to the cloud.

Finally, despite differences in the mixing state the temperature profile in the boundary layer very closely followed a dry adiabat in all three cases. This provides additional confirmation that the CBH should occur approximately at the LCL, as it does in Fig. 1e & 1f.

4.3 Mixing State Classification

Throughout the voyage, the correlation analysis showed that the boundary layer was either poorly-mixed, well-mixed, or contained fog (Fig. 1f), with the most commonly-observed state being the well-mixed boundary layer. The boundary layer was labeled 'well-mixed' if correlations were positive. It contained fog if the relative humidity was 100% or the CBH was lower than 50 m. Failing either criteria, the boundary layer was labeled 'poorly-mixed.' From these definitions, we optimized a decision-tree classification system to predict the state of boundary layer mixing. For predictor variables, we used the near-surface square of the Brunt-Väisälä frequency, N^2, and the wind speed, U_{10}.

We found that when the surface layer was stable ($\mathrm{N}^2 > 0$), fog was present. However, if the surface layer was unstable and either of the following conditions were met, then the boundary layer fell into the well-mixed category:

$$\begin{aligned} N^2 &\leq -1.5 \times 10^{-3} \ \mathrm{s}^{-2} \\ U_{10} &\geq 7.8 \ \mathrm{m\ s}^{-2} \end{aligned} \tag{4}$$

Otherwise, the boundary layer was poorly-mixed. In Fig. 3a these conditions are compared to the original data labels. We find that the criteria identified above provide sufficient, but not necessary conditions for a well-mixed boundary layer. Since, even in poorly-mixed conditions, the boundary layer was observed to be well-mixed 47% of the time. Similarly, a stable surface layer almost guaranteed the presence of fog, but was not necessary for it to be observed. For instance, from February 13$^{\mathrm{th}}$ to 17$^{\mathrm{th}}$ a semi-continuous fog was present in spite of near-surface instability. Despite these inconsistencies, the decision tree had an overall accuracy of 85% within our observation period.

We believe that the blending of the mixing state of the boundary layer across these thresholds is a result of air mass history. It is a well documented feature of the atmosphere that while the Richardson number must drop below a critical threshold for turbulence to initiate ($\mathrm{Ri}_g < 0.25$)(Taylor, 1931; Miles, 1961), the Richardson number of a turbulent system can pass back over this threshold and the system will remain turbulent, even for much higher values of Ri_g (Galperin et al., 2007). The resulting hysteresis leads to a large classification uncertainty in calm, near-neutral conditions. We believe our classification results are subject to this type of hysteresis.

4.4 Boundary Layer Mixing over the Wider Southern Ocean

To extrapolate our results to broader spatial and temporal scales, we used forecasts from AMPS to examine rates of occurrence of the various mixing states. The forecasts were validated against observations from radiosondes (Fig. 2; Table S1). Overall, the measurements and predictions of the variables of interest were very well-correlated and these relationships were highly statistically significant ($p < 0.001$).

A joint histogram presented in Fig. 3b shows how often different boundary layer states occurred over the Southern Ocean based on estimates from AMPS. Overall, forecasts predict that the boundary layer is well-mixed 49% of the time, poorly-mixed 8% of the time, and contains fog 43% of the time. Since the presence of fog implies a total coupling between boundary layer aerosol and cloud, this means that low-level cloud are potentially influenced by boundary layer particles 92% of the time.

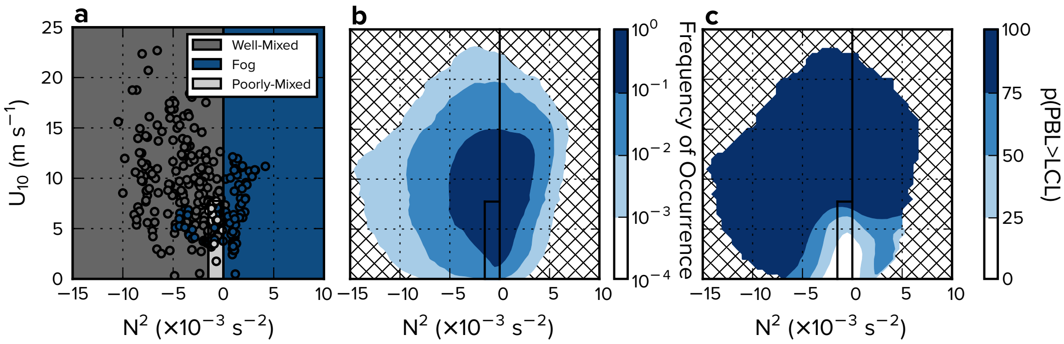

Figure 3. (a) The correlation analysis was used to decide whether the boundary layer was "well-mixed", "poorly-mixed", or if fog was present. Two variables, U_{10} and N^2, which describe the strength of turbulence from shear and instability, were used to classify these periods. (b) A joint histogram shows the frequency with which any combination of the bulk N^2 and U_{10} was predicted over the Southern Ocean by the Antarctic Mesoscale Prediction System (AMPS) within the February–March, 2018 period. Both land and coastal seas (<100 km) were masked. (c) The probability that the height of the planetary boundary layer (PBL) predicted by AMPS was deeper than the lifted condensation level (LCL).

We then calculated the probability that the planetary boundary layer (PBL) thickness exceeded the LCL under those conditions in Fig. 3c. As observed in Fig. 1e & 1f, CBH often occurred at the LCL. Comparing the thickness of the PBL to the LCL therefore gives us a good measure of aerosol–cloud coupling from AMPS. In unstable conditions, Fig. 3c agrees well with the threshold criteria in Eq. (4). It also gives a better sense of the hysteresis of turbulence. The predictions from AMPS suggest that while aerosol–cloud coupling can occur when the boundary layer stability drops below the threshold in Eq. (4), coupling is not guaranteed at low wind speeds until N^2 falls below -4$\times$10^{-3} s^{-2}. Similarly, near-surface winds must surpass 8 m s^{-1}; which is in agreement with Eq. (4).

In stable conditions, AMPS predicted that the PBL was not always guaranteed to be deeper than the LCL. However, when the atmosphere was stable, we only ever observed fog (Fig. 3a). This indicates that within AMPS, the PBL was virtually non-existent in calm, stable conditions. Overall, however, Fig. 3c confirms that the Southern Ocean boundary layer is consistently well-mixed.

5 Discussion

Overall, we found that correlations between the abundance of suspended particle surface area measured at sea-level and ceilometer backscatter were consistently high throughout our observation period in the Southern Ocean (Fig. 1f). Given this strong relationship, we can infer that turbulence, convection, or a combination of the two is continually mixing particles from sea level up to cloud base height to maintain these high correlations. As a result, the optical thickness of the overlying cloud, which is partially determined by cloud droplet number and cloud phase, is sensitive to both the abundance and physicochemical properties of the particles measured at the surface. This highlights the value of ship-based observations in aerosol–cloud interaction studies, as these measurements are relevant to understanding the detailed processes defining cloud formation and cloud properties in this region.

However, a well-mixed marine boundary layer is not always guaranteed, it is often stratified into a near-surface boundary layer and a sub-cloud layer (Garratt, 1994). Radiosondes launched from Macquarie Island (54.62°S, 158.85°E) over the past two decades found that the boundary layer was well-mixed just 17.8% of the time; further, clouds were only present within the mixed boundary layer 68% of this time (12% overall) (Hande, Siems, Manton, & Belusic, 2012). The correlation analysis and forecasts of occurrence from the Antaractic Mesoscale Prediction System (AMPS) we present here are thus markedly different. Forecasts from AMPS show that the boundary layer in the wider Southern Ocean region is well-mixed from sea-level to cloud base 92% of the time.

Part of the discrepancy between our results and previous radiosonde analyses may depend on whether weak temperature inversions prohibit mass transfer. Since, even in a stratified boundary layer it is still possible for boundary layer particulate to efficiently mix into overlying cloud. For example, in the Aerosol Characterization Experiment, wind shear within the sub-cloud layer was often strong enough to mix particulate from the boundary layer and into cloud (Russell et al., 1998). Indeed, Hande, Siems, Manton, and Belusic (2012) found that in half of the cases where the boundary layer was stratified by a temperature inversion, the layer overlying the boundary layer was significantly sheared. Here, we show that surface area correlations persist above inversions of at least 0.6 K km^{-1} (Fig. 1f & 2). Our correlation analysis is mostly sensitive to trends in the abundance of larger particles, which make up the bulk of suspended surface area. If these can be transferred across weak inversions, then smaller particles and water vapour are highly likely to be similarly mixed. Therefore, classifying the mixing state of the boundary layer based on correlations of particle surface area arguably provides a more robust definition of mixing than a thermodynamic analysis. As the boundary layer is typically in a well-mixed state, boundary-layer particulate are almost always available to low-lying cloud in the region.

We found that despite being readily-available to nascent clouds, sea spray particles were typically outnumbered by smaller, cloud-processed particles (Fig. 1c), consistent with previous studies. However, these particles are among the only ice-nucleating particles in the region (DeMott et al., 2016). Climate models that determine the primary nucleation of ice within low-level clouds according to the abundance of boundary layer ice-nucleating particles see large improvements in predictions for the opacity of clouds in the cold sector of Southern Ocean cyclones (Vergara-Temprado et al., 2018). This is a result of global climate models implicitly over-estimating the amount of ice formed during primary ice nucleation. While models must develop more realistic mechanisms for predicting cloud glaciation we have shown that low-level Southern Ocean clouds almost always have access to ice-nucleating particles in the boundary layer. Thus, they must also more carefully parameterize the flux of sea spray particles (Hartery et al., 2020).

6 Conclusions

In this work we presented a new technique for determining the state of boundary layer mixing based on the Spearman Rank correlation of sea-level observations of suspended particle surface area and ceilometer backscatter. Below-cloud, these correlations were often high, implying that particles measured at sea-level were well-mixed throughout the boundary layer and were therefore readily-available to nascent, low-level cloud. This agreed with our observation, and previous work across multiple voyages (Kuma et al., 2019), that the lifted condensation level generally coincides with cloud base height. This can only be true if water vapour, and as a result particulate, is well-mixed throughout the boundary layer. Finally, we expanded our time-series analysis into a regional analysis of boundary layer mixing by generating a simple boundary layer classification system. We found that the Southern Ocean boundary layer was well-mixed 92% of the time based on regional forecasts. Thus, in-situ, sea-level observations offer substantial insight into clouds over the Southern Ocean.

Acknowledgments

This project was funded through the New Zealand Deep South National Science Challenge Cloud and Aerosols project (2017–19). Voyage operations were supported through a New Zealand Crown Funding Agreement and associated voyage science was funded through the National Institute of Water and Atmospheric Research's Research Programme in Ocean-Climate Interactions (2017/19 SCI). S.H. acknowledges support from the University of Canterbury Doctoral Scholarship. Thanks to R/V *Tangaroa* Captain Evan Solly and crew for safe passage through the Ross Sea and installation of scientific equipment. Thanks to fellow sea-going scientific staff and voyage leader Dr David Bowden. Voyage data presented in this work will be archived to Zenodo. A corresponding voyage manuscript is in preparation.

References

Bates, T. S., Huebert, B. J., Gras, J. L., Griffiths, F. B., & Durkee, P. A. (1998). International global atmospheric chemistry (IGAC) project's first aerosol characterization experiment (ACE 1): Overview. *Journal of Geophysical Research: Atmospheres*, *103*(D13), 16297–16318.

Bigg, E. K., & Hopwood, S. C. (1963). Ice nuclei in the Antarctic. *Journal of the Atmospheric Sciences*, *20*(3), 185-188. doi: 10.1175/1520-0469(1963)020⟨0185:INITA⟩2.0.CO;2

Bodas-Salcedo, A., Williams, K. D., Ringer, M. A., Beau, I., Cole, J. N., Dufresne, J.-L., … Yokohata, T. (2014). Origins of the solar radiation biases over the Southern Ocean in CFMIP2 models. *Journal of Climate*, *27*(1), 41–56.

Boers, R., Jensen, J., & Krummel, P. (1998). Microphysical and short-wave radiative structure of stratocumulus clouds over the Southern Ocean: Summer results and seasonal differences. *Quarterly Journal of the Royal Meteorological Society*, *124*(545), 151–168.

Borys, R. D., Lowenthal, D. H., Cohn, S. A., & Brown, W. O. J. (2003). Mountaintop and radar measurements of anthropogenic aerosol effects on snow growth and snowfall rate. *Geophysical Research Letters*, *30*(10). doi: 10.1029/2002GL016855

DeMott, P. J., Hill, T. C. J., McCluskey, C. S., Prather, K. A., Collins, D. B., Sullivan, R. C., … Franc, G. D. (2016). Sea spray aerosol as a unique source of ice nucleating particles. *Proceedings of the National Academy of Sciences*, *113*(21), 5797–5803. doi: 10.1073/pnas.1514034112

Edson, J. B., Jampana, V., Weller, R. A., Bigorre, S. P., Plueddemann, A. J., Fairall, C. W., … Hersbach, H. (2013). On the exchange of momentum over the open ocean. *Journal of Physical Oceanography*, *43*(8), 1589–1610. doi: 10.1175/JPO-D-12-0173.1

Galperin, B., Sukoriansky, S., & Anderson, P. S. (2007). On the critical Richardson number in stably stratified turbulence. *Atmospheric Science Letters*, *8*(3), 65-69. doi: 10.1002/asl.153

Garratt, J. (1994). Review: the atmospheric boundary layer. *Earth-Science Reviews*, *37*(1), 89 - 134. doi: https://doi.org/10.1016/0012-8252(94)90026-4

Hande, L. B., Siems, S. T., & Manton, M. J. (2012). Observed trends in wind speed over the Southern Ocean. *Geophysical Research Letters*, *39*(11). doi: 10.1029/2012GL051734

Hande, L. B., Siems, S. T., Manton, M. J., & Belusic, D. (2012). Observations of wind shear over the Southern Ocean. *Journal of Geophysical Research: Atmospheres*, *117*(D12). doi: 10.1029/2012JD017488

Hartery, S., Toohey, D., Revell, L., Sellegri, K., Kuma, P., Harvey, M., & McDonald, A. J. (2020). Constraining the surface flux of sea spray particles from the Southern Ocean. *Journal of Geophysical Research: Atmospheres*, *125*(4). doi: 10.1029/2019JD032026

Haynes, J. M., Jakob, C., Rossow, W. B., Tselioudis, G., & Brown, J. (2011). Major characteristics of Southern Ocean cloud regimes and their effects on the energy budget. *Journal of Climate*, *24*(19), 5061-5080. doi: 10.1175/2011JCLI4052.1

Hegg, D. A., Covert, D. S., Jonsson, H. H., & Woods, R. (2009). Differentiating natural and anthropogenic cloud condensation nuclei in the California coastal zone. *Tellus B: Chemical and Physical Meteorology*, *61*(4), 669-676. doi: 10.1111/j.1600-0889.2009.00435.x

Hoppel, W. A., Frick, G. M., & Larson, R. E. (1986). Effect of nonprecipitating clouds on the aerosol size distribution in the marine boundary layer. *Geophysical Research Letters*, *13*(2), 125-128. doi: 10.1029/GL013i002p00125

Hu, Y., Rodier, S., Xu, K.-m., Sun, W., Huang, J., Lin, B., … Josset, D. (2010). Occurrence, liquid water content, and fraction of supercooled water clouds from combined CALIOP/IIR/MODIS measurements. *Journal of Geophysical Research: Atmospheres*, *115*(D4).

Irving, D., Simmonds, I., & Keay, K. (2010). Mesoscale cyclone activity over the ice-free Southern Ocean: 1999–2008. *Journal of Climate*, *23*(20), 5404-5420. doi: 10.1175/2010JCLI3628.1

Janjić, Z. I. (2001). *Nonsingular implementation of the Mellor-Yamada level 2.5 scheme in the NCEP Meso model* (Office Note No. 437). NOAA Institutional Repository: National Center for Environmental Prediction (NCEP).

Jin, Y., Sugimoto, N., Shimizu, A., Nishizawa, T., Kai, K., Kawai, K., … Wille, H. (2018). Evaluation of ceilometer attenuated backscattering coefficients for aerosol profile measurement. *Journal of Applied Remote Sensing*, *12*(4), 1-12. doi: 10.1117/1.JRS.12.042604

Jolly, B., McDonald, A. J., Coggins, J. H. J., Zawar-Reza, P., Cassano, J., Lazzara, M., … Dale, E. (2016). A validation of the Antarctic mesoscale prediction system using self-organizing maps and high-density observations from SNOWWEB. *Monthly Weather Review*, *144*(9), 3181-3200. doi: 10.1175/MWR-D-15-0447.1

Korhonen, H., Carslaw, K. S., Forster, P. M., Mikkonen, S., Gordon, N. D., & Kokkola, H. (2010). Aerosol climate feedback due to decadal increases in southern hemisphere wind speeds. *Geophysical Research Letters*, *37*(2). doi: 10.1029/2009GL041320

Kuma, P., McDonald, A. J., Morgenstern, O., Alexander, S. P., Cassano, J. J., Garrett, S., … Williams, J. (2019). Evaluation of Southern Ocean cloud in the HadGEM3 general circulation model and MERRA-2 reanalysis using ship-based observations. *Atmospheric Chemistry and Physics Discussions*, *2019*, 1–37. doi: 10.5194/acp-2019-201

McCoy, D. T., Burrows, S. M., Wood, R., Grosvenor, D. P., Elliott, S. M., Ma, P.-L., … Hartmann, D. L. (2015). Natural aerosols explain seasonal and spatial patterns of Southern Ocean cloud albedo. *Science Advances*, *1*(6). doi: 10.1126/sciadv.1500157

Miles, J. W. (1961). On the stability of heterogeneous shear flows. *Journal of Fluid Mechanics*, *10*(4), 496–508. doi: 10.1017/S0022112061000305

Modini, R. L., Frossard, A. A., Ahlm, L., Russell, L. M., Corrigan, C. E., Roberts, G. C., … Leaitch, W. R. (2015). Primary marine aerosol-cloud interactions off the coast of California. *Journal of Geophysical Research: Atmospheres*, *120*(9), 4282-4303. doi: 10.1002/2014JD022963

Prather, K. A., Bertram, T. H., Grassian, V. H., Deane, G. B., Stokes, M. D., De-

Mott, P. J., … Zhao, D. (2013). Bringing the ocean into the laboratory to probe the chemical complexity of sea spray aerosol. *Proceedings of the National Academy of Sciences*, *110*(19), 7550–7555. doi: 10.1073/pnas.1300262110

Quinn, P. K., Coffman, D. J., Johnson, J. E., Upchurch, L. M., & Bates, T. S. (2017). Small fraction of marine cloud condensation nuclei made up of sea spray aerosol. *Nature Geoscience*, *10*, 674–679. doi: 10.1038/ngeo3003

Richardson, L. F. (1920). The supply of energy from and to atmospheric eddies. *Proceedings of the Royal Society of London*, *97*(686), 354–373.

Romps, D. M. (2017). Exact expression for the lifting condensation level. *Journal of the Atmospheric Sciences*, *74*(12), 3891-3900. doi: 10.1175/JAS-D-17-0102.1

Russell, L. M., Lenschow, D. H., Laursen, K. K., Krummel, P. B., Siems, S. T., Bandy, A. R., … Bates, T. S. (1998). Bidirectional mixing in an ACE 1 marine boundary layer overlain by a second turbulent layer. *Journal of Geophysical Research: Atmospheres*, *103*(D13), 16411–16432.

Schluessel, P., Emery, W. J., Grassl, H., & Mammen, T. (1990). On the bulk-skin temperature difference and its impact on satellite remote sensing of sea surface temperature. *Journal of Geophysical Research: Oceans*, *95*(C8), 13341-13356. doi: 10.1029/JC095iC08p13341

Schuddeboom, A., Varma, V., McDonald, A. J., Morgenstern, O., Harvey, M., Parsons, S., … Furtado, K. (2019). Cluster-based evaluation of model compensating errors: A case study of cloud radiative effect in the Southern Ocean. *Geophysical Research Letters*, *46*(6), 3446-3453. doi: 10.1029/2018GL081686

Taylor, G. I. (1931). Effect of variation in density on the stability of superposed streams of fluid. *Proceedings of the Royal Society of London*, *132*(820), 499–523.

Twomey, S. (1977). The influence of pollution on the shortwave albedo of clouds. *Journal of the Atmospheric Sciences*, *34*(7), 1149-1152. doi: 10.1175/1520-0469(1977)034⟨1149:TIOPOT⟩2.0.CO;2

Vergara-Temprado, J., Miltenberger, A. K., Furtado, K., Grosvenor, D. P., Shipway, B. J., Hill, A. A., … Carslaw, K. S. (2018). Strong control of Southern Ocean cloud reflectivity by ice-nucleating particles. *Proceedings of the National Academy of Sciences*, *115*(11), 2687–2692. doi: 10.1073/pnas.1721627115

Wofsy, S. C. (2011). HIAPER pole-to-pole observations (HIPPO): fine-grained, global-scale measurements of climatically important atmospheric gases and aerosols. *Philosophical Transactions of the Royal Society*, *369*(1943), 2073-2086. doi: 10.1098/rsta.2010.0313

Young, I. R., Zieger, S., & Babanin, A. V. (2011). Global trends in wind speed and wave height. *Science*, *332*(6028), 451–455. doi: 10.1126/science.1197219